Electronic properties of a biased graphene bilayer

Eduardo V Castro[1,2]**, K S Novoselov**[3]**, S V Morozov**[3]**, N M R Peres**[4]**,
J M B Lopes dos Santos**[1]**, Johan Nilsson**[5]**, F Guinea**[2]**, A K Geim**[3]
and A H Castro Neto[5]

[1] CFP and Departamento de Física, Faculdade de Ciências Universidade do Porto,
P-4169-007 Porto, Portugal
[2] Instituto de Ciencia de Materiales de Madrid, CSIC, Cantoblanco, E-28049 Madrid, Spain
[3] Department of Physics and Astronomy, University of Manchester, Manchester M13 9PL, UK
[4] Centre of Physics and Departamento de Física, Universidade do Minho, P-4710-057 Braga,
Portugal
[5] Department of Physics, Boston University, 590 Commonwealth Avenue, Boston, MA 02215,
USA

Abstract
We study, within the tight-binding approximation, the electronic properties of a graphene
bilayer in the presence of an external electric field applied perpendicular to the system—a
biased bilayer. The effect of the perpendicular electric field is included through a parallel plate
capacitor model, with screening correction at the Hartree level. The full tight-binding
description is compared with its four-band and two-band continuum approximations, and the
four-band model is shown to always be a suitable approximation for the conditions realized in
experiments. The model is applied to real biased bilayer devices, made out of either SiC or
exfoliated graphene, and good agreement with experimental results is found, indicating that the
model is capturing the key ingredients, and that a finite gap is effectively being controlled
externally. Analysis of experimental results regarding the electrical noise and cyclotron
resonance further suggests that the model can be seen as a good starting point for understanding
the electronic properties of graphene bilayer. Also, we study the effect of electron–hole
asymmetry terms, such as the second-nearest-neighbour hopping energies t' (in-plane) and γ_4
(inter-layer), and the on-site energy Δ.

(Some figures in this article are in colour only in the electronic version)

1. Introduction

The double-layer graphene system—the so-called bilayer
graphene (BLG)—is now a subject of considerable interest due
to its unusual properties [1–4], dissimilar to a great extent to
those of single-layer graphene (SLG) [5]. The integer quantum
Hall effect (QHE) is a paradigmatic case; characterized by
the absence of a plateau at the Dirac point [6], and hence
anomalous, it is associated with massive Dirac fermions and
two zero-energy modes [7].

One of the most remarkable properties of BLG is the
ability to open a gap in the spectrum by electric field effect—
biased BLG [7]. This has been shown both experimentally
and theoretically, providing the first semiconductor with an
externally tunable gap [8–17]. In the absence of an external

perpendicular electric field—unbiased BLG—the system is
characterized by four bands, two of them touching each
other parabolically at zero energy, and giving rise to the
massive Dirac fermions mentioned above, and the other two
separated by an energy $\pm t_\perp$. Hence, an unbiased BLG is a
two-dimensional zero-gap semiconductor [7, 6, 18]. At the
neutrality point the conductivity shows a minimum of the
order of the conductance quantum [6, 19–23, 18, 24, 25], a
property shared with SLG [26]. This prevents standard device
applications where the presence of a finite gap producing high
on–off current ratios is of paramount importance. The fact
that a simple perpendicular electric field is enough to open
a gap, and even more remarkable, to control its size, clearly
demonstrates the potential of this system for carbon-based
electronics use [27, 28].

The biased BLG reveals interesting properties on its own. The gap has been shown to be robust in the presence of disorder [29–31], induced either by impurities or dilution, but is completely absent in rotated (non-AB-stacked) bilayers, where the SLG linear dispersion is recovered [32, 33]. The band structure near the gap shows a 'Mexican hat' like behaviour, with a low doping Fermi surface which is a ring [11]. Such a topologically nontrivial Fermi surface leads to an enhancement of electron–electron interactions, and to a ferromagnetic instability at low enough density of carriers [34, 35]. In the presence of a perpendicular magnetic field, the biased BLG shows cyclotron mass renormalization and an extra plateau at zero Hall conductivity, signalling the presence of a sizable gap at the neutrality point [12, 10, 36]. Gaps can also be induced in stacks with more than two layers as long as the stacking order is of the rhombohedral type [11, 14], although screening effects may become important in doped systems with increasing number of layers [15]. Recently, a ferromagnetic proximity effect was proposed as a different mechanism which can also open a gap in the spectrum of the BLG, leading to a sizable magnetoresistive effect [37]. Strain applied to the biased BLG has also shown to produce further gap modulation [38].

In this paper the electronic properties of a biased BLG are studied within a full tight-binding model, which enables the analysis of the whole bandwidth, validating previous results obtained using low energy effective models. The screening of the applied perpendicular electric field is obtained within a self-consistent Hartree approach, and a comparison with experiments is provided. The effect of the bias in the cyclotron mass and cyclotron resonance is addressed, and the results are shown to agree well with experimental measurements.

The paper is organized as follows. In section 2 the lattice structure of BLG and the tight-binding Hamiltonian are presented; bulk electronic properties are discussed in section 3, with particular emphasis on the screening correction; the effect of a perpendicular magnetic field is studied in section 4; section 5 contains our conclusions. We have also included three appendices: appendix A provides details on the calculation of the density asymmetry between layers for a finite bias; in appendix B we give the analytical expression for the biased BLG density of states, valid over the entire energy spectrum; analytical expressions for the cyclotron mass obtained within the full tight-binding model are given in appendix C.

2. The model

Here we consider only AB Bernal stacking, where the top layer has its A sublattice on top of sublattice B of the bottom layer. We use indices 1 and 2 to label the top and bottom layer, respectively. The unit cell of a bilayer has twice the number of atoms of a single layer, and the basis vectors may be written as $\mathbf{a}_1 = a\,\hat{\mathrm{e}}_x$ and $\mathbf{a}_2 = a(\hat{\mathrm{e}}_x - \sqrt{3}\,\hat{\mathrm{e}}_y)/2$, where $a = 2.46$ Å.

In the tight-binding approximation, the in-plane hopping energy, t, and the inter-layer hopping energy, $t_\perp$, define the most relevant energy scales. The simplest tight-binding

Table 1. Tight-binding parameter values γ_3 [41, 48], γ_4 [41, 49, 48], Δ [49, 50, 48], and t' [51], in units of the in-plane hopping t.

γ_3	γ_4	Δ	t'
0.03–0.1	0.04–0.07	0.005–0.008	~0.04

Hamiltonian describing non-interacting π-electrons in BLG reads

$$H_{\mathrm{TB}} = \sum_{i=1}^{2} H_i + t_\perp \sum_{\mathbf{R},\sigma} \left[a_{1,\sigma}^\dagger(\mathbf{R}) b_{2,\sigma}(\mathbf{R}) + \mathrm{h.c.} \right] + H_V, \quad (1)$$

with the SLG Hamiltonian

$$H_i = -t \sum_{\mathbf{R},\sigma} \left[a_{i,\sigma}^\dagger(\mathbf{R}) b_{i,\sigma}(\mathbf{R}) + a_{i,\sigma}^\dagger(\mathbf{R}) b_{i,\sigma}(\mathbf{R} - \mathbf{a}_1) \right.$$
$$\left. + a_{i,\sigma}^\dagger(\mathbf{R}) b_{i,\sigma}(\mathbf{R} - \mathbf{a}_2) + \mathrm{h.c.} \right], \quad (2)$$

where $a_{i,\sigma}(\mathbf{R})$ [$b_{i,\sigma}(\mathbf{R})$] is the annihilation operator for electrons at position $\mathbf{R}$ in sublattice Ai (Bi), $i = 1, 2$, and spin σ. The in-plane hopping t can be inferred from the Fermi velocity in graphene $v_{\mathrm{F}} = ta\hbar^{-1}\sqrt{3}/2 \approx 10^6$ ms^{-1} [39], yielding $t \approx 3.1$ eV, in good agreement with what is found experimentally for graphite [40]. This value also agrees with a recent Raman scattering study of the electronic structure of BLG [41]. As regards the inter-layer hopping $t_\perp$, angle-resolved photoemission spectroscopy (ARPES) measurements on epitaxial BLG give $t_\perp \approx 0.43$ eV [8], and Raman scattering for BLG obtained by micromechanical cleavage of graphite yields $t_\perp \approx 0.30$ eV [41]. The experimental value for bulk graphite is $t_\perp \approx 0.39$ eV [42], which means that for practical purposes we can always assume $t_\perp/t \sim 0.1 \ll 1$. These values for t and $t_\perp$ compare fairly well with what is obtained from first-principles calculations for graphite [43] using the well established Slonczewski–Weiss–McClure (SWM) parametrization model [44, 45] to fit the bands near the Fermi energy. The SWM model assumes extra parameters that can also be incorporated in a tight-binding model for BLG, namely, the inter-layer second-NN hoppings γ_3 and γ_4, where γ_3 connects different sublattices (B1–A2) and γ_4 equal sublattices (A1–A2 and B1–B2). Additionally, there is an on-site energy Δ reflecting the inequivalence between sublattices A1, B2 and B1, A2—the former project exactly on top of each other while the latter lie on the hexagon centre of the other layer. The consequences of these extra terms for the band structure obtained from (1) are well known: γ_3 induces trigonal warping and both γ_4 and Δ give rise to electron–hole asymmetry [46, 7, 47]. The in-plane second-NN hopping energy t' is not considered in the usual tight-binding parametrization of the SWM model. Nevertheless, this term can have important consequences since it breaks particle–hole symmetry but does not modify the Dirac spectrum. Typical values are given in table 1 as obtained in recent experiments, except for t' quoted from density functional theory (DFT) calculations.

We are interested in the properties of BLG in the presence of a perpendicular electric field—the biased BLG. The effect of the induced energy difference between layers, parametrized

by V, may be accounted for by adding H_V, the last term in (1), with H_V given by

$$H_V = \frac{V}{2} \sum_{\mathbf{R},\sigma} \left[n_{A1}(\mathbf{R}) + n_{B1}(\mathbf{R}) - n_{A2}(\mathbf{R}) - n_{B2}(\mathbf{R}) \right], \quad (3)$$

where $n_{Ai}(\mathbf{R})$ and $n_{Bi}(\mathbf{R})$ are number operators.

3. Bulk electronic properties

Introducing the Fourier components $a_{i,\sigma,\mathbf{k}}$ and $b_{i,\sigma,\mathbf{k}}$ of operators $a_{i,\sigma}(\mathbf{R})$ and $b_{i,\sigma}(\mathbf{R})$, respectively, with the layer index $i = 1, 2$, we can rewrite (1) as $H = \sum_{\mathbf{k},\sigma} \psi^\dagger_{\sigma,\mathbf{k}} H_{\mathbf{k}} \psi_{\sigma,\mathbf{k}}$, where $\psi^\dagger_{\sigma,\mathbf{k}} = [a^\dagger_{1,\sigma,\mathbf{k}}, b^\dagger_{1,\sigma,\mathbf{k}}, a^\dagger_{2,\sigma,\mathbf{k}}, b^\dagger_{2,\sigma,\mathbf{k}}]$ is a four-component spinor, and $H_{\mathbf{k}}$ is given by

$$H_{\mathbf{k}} = \begin{pmatrix} V/2 & -ts_{\mathbf{k}} & 0 & -t_\perp \\ -ts^*_{\mathbf{k}} & V/2 & 0 & 0 \\ 0 & 0 & -V/2 & -ts_{\mathbf{k}} \\ -t_\perp & 0 & -ts^*_{\mathbf{k}} & -V/2 \end{pmatrix}. \quad (4)$$

The factor $s_{\mathbf{k}} = 1 + e^{i\mathbf{k}\cdot\mathbf{a}_1} + e^{i\mathbf{k}\cdot\mathbf{a}_2}$ determines the matrix elements for the SLG Hamiltonian in reciprocal space ($t_\perp = 0$, $V = 0$), from which the SLG dispersion is obtained, $\epsilon_{\mathbf{k}} = \pm t|s_{\mathbf{k}}|$. The resultant conduction ($+$) and valence ($-$) bands touch each other in a conical way at the corners of the first Brillouin zone (BZ), the K and K′ points [5]. This touching occurs at zero energy, the Fermi energy for undoped graphene. The four-band continuum approximation for (4), valid at energy scales $E \ll t$, may be obtained by introducing the small wavevector $\mathbf{q}$ which measures the difference between $\mathbf{k}$ and the corners of the BZ. Linearizing the factor $s_{\mathbf{k}}$ around the K points we can rewrite (4) as

$$H_K = \begin{pmatrix} V/2 & v_F p e^{-i\varphi_{\mathbf{p}}} & 0 & -t_\perp \\ v_F p e^{i\varphi_{\mathbf{p}}} & V/2 & 0 & 0 \\ 0 & 0 & -V/2 & v_F p e^{-i\varphi_{\mathbf{p}}} \\ -t_\perp & 0 & v_F p e^{i\varphi_{\mathbf{p}}} & -V/2 \end{pmatrix}, \quad (5)$$

where $\mathbf{p} = \hbar\mathbf{q}$ and $\varphi_{\mathbf{p}} = \tan^{-1}(p_y/p_x)$. Around the K′ points, (5) with complex conjugate matrix elements defines $H_{K'}$ [52, 7].

Equation (5) can be further simplified if one assumes $v_F p, V \ll t_\perp$. By eliminating high energy states perturbatively we can write a two-band effective Hamiltonian describing low energy states whose electronic amplitude is mostly localized on B1 and A2 sites. Near the K points the resulting Hamiltonian may be written as

$$H_{\text{eff}} = -\begin{pmatrix} -V/2 & e^{i2\varphi_{\mathbf{p}}} v_F^2 p^2/t_\perp \\ e^{-i2\varphi_{\mathbf{p}}} v_F^2 p^2/t_\perp & V/2 \end{pmatrix}, \quad (6)$$

whereas the complex conjugate matrix elements should be taken for a low energy description around the K′ points. The two-component wavefunctions have the form $\Phi = (\phi_{B1}, \phi_{A2})$ [52, 7, 53].

In the following we discuss the electronic structure resulting from the tight-binding Hamiltonian (4), and comment on the approximations given above by (5) and (6).
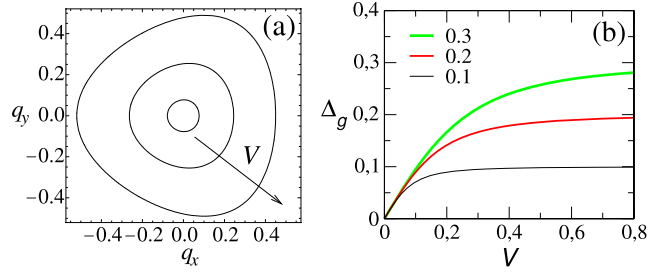

Figure 1. (a) Solution of (8) for $V = t_\perp/2, 2t_\perp, 4t_\perp$. (b) Δ_g versus V for various $t_\perp$ values. Energy is given in units of t and momentum in units of a^{-1}.

3.1. The electronic structure

Let us briefly discuss the electronic structure of the biased BLG using the full tight-binding Hamiltonian given by (1). The spectrum of (1) for $V \neq 0$ reads

$$E^{\pm\pm}_{\mathbf{k}}(V) = \pm\sqrt{\epsilon_{\mathbf{k}}^2 + \frac{t_\perp^2}{2} + \frac{V^2}{4} \pm \sqrt{t_\perp^4/4 + (t_\perp^2 + V^2)\epsilon_{\mathbf{k}}^2}}. \quad (7)$$

As can be seen from (7), the $V = 0$ gapless system turns into a semiconductor with a gap controlled by V. Moreover, the two bands close to zero energy are deformed near the corners of the BZ [5], so the minimum of $|E^{\pm-}_{\mathbf{k}}(V)|$ no longer occurs at these corners. As a consequence, the low doping Fermi surface is completely different from the $V = 0$ case, with its shape controlled by V.

It can be readily shown that the minimum of sub-band $E^{+-}_{\mathbf{k}}(V)$ (or equivalently, the maximum of $E^{--}_{\mathbf{k}}(V)$) occurs for all $\mathbf{k}$s satisfying

$$\epsilon_{\mathbf{k}}^2 = \alpha(V, t_\perp), \quad (8)$$

with $\alpha(V, t_\perp) = (V^4/4 + t_\perp^2 V^2/2)/(V^2 + t_\perp^2)$—note that $\partial E^{\pm-}_{\mathbf{k}}/\partial\epsilon_{\mathbf{k}} = 0$ at the desired extrema. Equation (8) has solutions for $\sqrt{\alpha} \leqslant 3t$ ($3t$ is half of the single-layer bandwidth). When $\sqrt{\alpha} > 3t$, the minimum of $E^{+-}_{\mathbf{k}}(V)$ occurs at the Γ point. Figure 1(a) shows the solution of (8) around the K point for $V = t_\perp/2, 2t_\perp, 4t_\perp$ (around the K′ point the figure is rotated by $\pi/3$). At low doping the Fermi sea acquires a line shape given by the solution of (8), the linewidth being determined by the doping level. As can be seen in figure 1(a), when $V < t_\perp$ the Fermi sea approaches a ring, the Fermi ring, centred at the BZ corners [11, 34]. As V is increased there is an apparent trigonal distortion showing up, which originates from the single-layer dispersion in (8).

The existence of a Fermi ring is easily understood using the continuum version of (7), i.e., the eigenvalues of (5). This amounts to substituting the single-layer dispersion in (7) by $v_F p$, which immediately implies cylindrical symmetry around K and K′. If we further assume that $v_F p \ll V \ll t_\perp$ holds, then (7) is well approximated by the 'Mexican hat' dispersion [11],

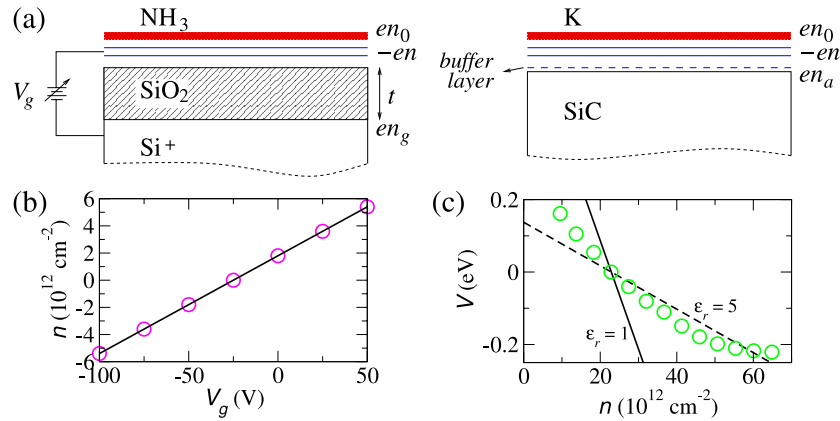$$E^{\pm-}(V) \approx \pm\frac{V}{2} \mp \frac{V v_F^2}{t_\perp^2} p^2 \pm \frac{v_F^4}{t_\perp^2 V} p^4, \quad (9)$$

Figure 2. (a) Biased BLG devices. (b) n versus V_g for the left device shown in (a): experimental data are shown as symbols [10]; the line is a linear fit with (14). (c) V versus n for the right BLG device shown in (a): symbols are experimental data from [8]; the lines are the result from (16).

which explains the Fermi ring. If, instead, we have $V < v_F p \ll t_\perp$, we can approximate (7) by

$$E^{\pm -}(V) \approx \pm \sqrt{V^2/4 + v_F^4 p^4/t_\perp^2}, \qquad (10)$$

which corresponds exactly to the eigenvalues of the effective two-band Hamiltonian in (6). Note that no continuum approximation can produce the trigonal distortion shown in figure 1(a).

The gap between conduction and valence bands, Δ_g, is twice the minimum value of $E_{\mathbf{k}}^{+-}(V)$ due to electron–hole symmetry, and is given by

$$\Delta_g = \begin{cases} \sqrt{t_\perp^2 V^2/(t_\perp^2 + V^2)}, & V \lesssim V_c \\ 2t \sqrt{9 + \dfrac{t_\perp^2}{2t^2} + \dfrac{V^2}{4t^2} - \sqrt{\dfrac{t_\perp^4}{4t^4} + 9\dfrac{t_\perp^2 + V^2}{t^2}}}, \\ & V > V_c, \end{cases} \qquad (11)$$

where $V_c = [18t^2 - t_\perp^2 + (18^2 t^4 + t_\perp^4)^{1/2}]^{1/2} \simeq 6t$, the approximation being valid for $t_\perp \ll t$. From (11) it can be seen that for both $V \ll t_\perp$ and $V \gg t$ one finds $\Delta_g \sim V$. However, there is a region for $t_\perp \lesssim V \lesssim 6t$ where the gap shows a plateau $\Delta_g \sim t_\perp$, as depicted in figure 1(b). The plateau ends when $V \simeq 6t$ (not shown).

3.2. Screening of the external field

So far we have considered V, i.e. the electrostatic energy difference between layers felt by a single electron, as a band parameter that controls the gap. However, the parameter V can be related to the perpendicular electric field applied to the BLG, avoiding the introduction of an extra free parameter in the present theory.

Let us call $\mathbf{E} = E\hat{e}_z$ the perpendicular electric field felt by electrons in BLG. The corresponding electrostatic energy $U(z)$ for an electron of charge $-e$ is related to the electric field as $eE = \partial U(z)/\partial z$, and thus V is given by

$$V = U(z_1) - U(z_2) = eEd, \qquad (12)$$

where z_1 and z_2 are the positions of layers 1 and 2, respectively, and $d \equiv z_1 - z_2 = 3.4$ Å is the inter-layer distance. Given the experimental conditions, the value of E can be calculated under a few assumptions, as detailed in the following.

3.2.1. The external field in real systems. If we assume the electric field E in (12) to be due exclusively to the external electric field applied to the BLG, $E = E_{ext}$, all we need in order to know V is the value of E_{ext},

$$V = eE_{ext}d. \qquad (13)$$

The experimental realization of a biased BLG has been achieved in epitaxial BLG through chemical doping [8, 54] and in back gated exfoliated BLG [10, 9]. In either case the value of E_{ext} can be extracted assuming a simple parallel plate capacitor model.

In the case of exfoliated BLG, devices are prepared by micromechanical cleavage of graphite on top of an oxidized silicon wafer (300 nm of SiO$_2$), as shown in the left panel of figure 2(a). A back gate voltage V_g applied between the sample and the Si wafer induces charge carriers due to the electric field effect, resulting in carrier densities $n_g = \beta V_g$ relatively to half-filling ($n_g > 0$ for electrons and $n_g < 0$ for holes). The geometry of the resulting capacitor determines the coefficient β. In particular, the electric field inside the oxidized layer is $E_{ox} = en_g/(\varepsilon_{SiO_2}\varepsilon_0)$, where ε_{SiO_2} and ε_0 are the permittivities of SiO$_2$ and free space, respectively. This implies a gate voltage $V_g = en_g t/(\varepsilon_{SiO_2}\varepsilon_0)$, from which we obtain the coefficient $\beta = \varepsilon_{SiO_2}\varepsilon_0/(et)$. For a SiO$_2$ thickness $t = 300$ nm and a dielectric constant $\varepsilon_{SiO_2} = 3.9$ we obtain $\beta \cong 7.2 \times 10^{10}$ cm^{-2} V^{-1}, which is in agreement with the values found experimentally [39, 55, 6]. In order to control independently the gap value and the Fermi level, in [10] the devices have been chemically doped by deposition of NH$_3$ on top of the upper layer, which adsorbed on graphene and effectively acted as a top gate providing a fixed electron density n_0 [56]. Charge conservation then implies a total density n in BLG given by $n = n_g + n_0$, or in terms of the applied gate

voltage,

$$n = \beta V_{\text{g}} + n_0. \qquad (14)$$

In figure 2(b) the charge density in BLG is shown as a function of V_{g}. The symbols are the experimental result obtained from Hall effect measurements [10], and the line is a linear fit with (14). The fit provides n_0, which for this particular experimental realization is $n_0 \simeq 1.8 \times 10^{12} \text{ cm}^{-2}$, and validates the parallel plate capacitor model applied to the back gate, since the fitted $\beta \simeq 7.2 \times 10^{10} \text{ cm}^{-2} \text{ V}^{-1}$ is in excellent agreement with the theoretical value. Extending the parallel plate capacitor model to include the effect of dopants, the external field E_{ext} is the result of charged surfaces placed above and below BLG. The accumulation or depletion layer in the Si wafer contributes with an electric field $E_{\text{b}} = en_{\text{g}}/(2\varepsilon_{\text{r}}\varepsilon_0)$, while dopants above BLG effectively provide the second charged surface with electric field $E_{\text{t}} = -en_0/(2\varepsilon_{\text{r}}\varepsilon_0)$. A relative dielectric constant ε_{r} different from unity may be attributed to the presence of SiO$_2$ below and vacuum on top, which gives $\varepsilon_{\text{r}} \approx (\varepsilon_{\text{SiO}_2} + 1)/2 \approx 2.5$, a value that can be slightly different due to adsorption of water molecules [56, 57]. Adding the two contributions, $E_{\text{ext}} = E_{\text{b}} + E_{\text{t}}$, and making use of the charge conservation relation, we arrive at an electrostatic energy difference V (see (13)) that depends linearly on the BLG density,

$$V = \left(\frac{n}{n_0} - 2 \right) \frac{e^2 n_0 d}{2\varepsilon_{\text{r}}\varepsilon_0}. \qquad (15)$$

In treating the dopants as a homogeneous charged layer we ignore possible lattice distortion induced by adsorbed molecules, as well as the electric field due to the NH$_3$ electric dipole, which may contribute to the gap in the spectrum. However, it has been shown recently [58] that for NH$_3$ these effects counteract, giving rise to a much smaller gap than other dopant molecules [59], for instance NH$_2$ and CH$_3$. For the biased BLG realized in [9], independence of the Fermi level and carrier density was achieved with a real top gate, which makes the parallel plate capacitor model a suitable approximation in that case.

In the case of epitaxial BLG, devices are grown on SiC by thermal decomposition of the Si face. (For the C face, the presence of rotational stacking faults prevents the usual AB Bernal stacking [60, 33].) The substrate is fixed (SiC), and graphene behaviour develops for carbon layers above the buffer layer [61–64], as schematically shown in the right panel of figure 2(a). Due to charge transfer from substrate to film, the as-prepared BLG devices appear electron doped with density n_{a}. First-principles calculations indicate that such doping is coming from interface states that develop between the buffer layer and the Si-terminated substrate [61, 62]. (Scanning tunnelling microscopy (STM) measurements corroborate the presence of interface states [65–67, 64].) From the point of view of our theoretical approach, we may interpret these interface states as an effective depletion layer that provides the external electric field necessary to make the system a biased BLG. In [8] the BLG density n was varied by doping the system with potassium (K) on top of the upper layer (see figure 2(a)), which originates an additional charged layer contributing to the external electric field. Applying the same

parallel plate capacitor model as before, we get an electrostatic energy difference that can be written as

$$V = \left(2 - \frac{n}{n_{\text{a}}} \right) \frac{e^2 n_{\text{a}} d}{2\varepsilon_{\text{r}}\varepsilon_0}. \qquad (16)$$

Following a similar reasoning to that of the case of exfoliated graphene on top of SiO$_2$, we would write $\varepsilon_{\text{r}} \approx (\varepsilon_{\text{SiC}} + 1)/2 \approx 5$. However, this value neglects that interface states (the effective bottom plate capacitor) occur above the SiC substrate, close to the graphene system, and thus $\varepsilon_{\text{r}} \approx 1$ should be more appropriate. In figure 2(c) we compare (16) with experimental results for V obtained by fitting ARPES measurements from [8]. For this particular biased BLG realization, the as-prepared carrier density was $n_{\text{a}} \approx 10^{13} \text{ cm}^{-2}$. From (16) this n_{a} value implies a zero V, i.e., zero electric field and therefore zero gap, for the bilayer density $n^{\text{th}} \approx 2 \times 10^{13} \text{ cm}^{-2}$. Experimentally, a zero gap was found around $n^{\text{exp}} \approx 2.3 \times 10^{13} \text{ cm}^{-2}$. Given the simplicity of the theory, it can be said that n^{th} and n^{exp} are in good agreement. However, the agreement is only good at $V \sim 0$, since the measured V is not a linear function of n, as (16) implies. In what follows we analyse in detail the effect of screening and how it modifies (15) and (16).

3.2.2. The screening correction. In deriving (15) and (16) we assumed that the electric field E in the BLG region was exactly the external one, E_{ext}. There is, however, an obvious additional contribution: the external electric field polarizes the BLG, inducing some charge asymmetry between the two graphene layers, which in turn gives rise to an internal electric field, E_{int}, that screens the external one.

To estimate E_{int} we can again apply a parallel plate capacitor model. The internal electric field due to the charge asymmetry between planes may thus be written as

$$E_{\text{int}} = \frac{e\Delta n}{2\varepsilon_{\text{r}}\varepsilon_0}, \qquad (17)$$

where $-e\Delta n$ is the induced charge imbalance between layers, which can be estimated through the weight of the wavefunctions in each layer,

$$\Delta n = n_1 - n_2 = \frac{2}{N_{\text{c}} A_{\bigcirc}} \sum_{j,l=\pm} {\sum_{\mathbf{k}}}'$$
$$\left(|\varphi_{\text{A1},\mathbf{k}}^{jl}|^2 + |\varphi_{\text{B1},\mathbf{k}}^{jl}|^2 - |\varphi_{\text{A2},\mathbf{k}}^{jl}|^2 - |\varphi_{\text{B2},\mathbf{k}}^{jl}|^2 \right), \qquad (18)$$

where the factor 2 comes from spin degeneracy, N_{c} is the number of unit cells and $A_{\bigcirc} = a^2 \sqrt{3}/2$ is the unit cell area, jl is a band label, and the prime sum runs over all occupied $\mathbf{k}$s in the first BZ. The amplitudes $\varphi_{\text{A}i,\mathbf{k}}^{jl}$ and $\varphi_{\text{B}i,\mathbf{k}}^{jl}$, with $i = 1, 2$, are determined by diagonalization of (4), enabling Δn to be written as

$$\Delta n = \frac{2}{N_{\text{c}} A_{\bigcirc}} \sum_{j,l=\pm} {\sum_{\mathbf{k}}}'$$
$$\frac{(\epsilon_{\mathbf{k}}^2 + \mathcal{K}_{\mathbf{k},-}^{jl})(\epsilon_{\mathbf{k}}^2 - \mathcal{K}_{\mathbf{k},+}^{jl})^2 - (\epsilon_{\mathbf{k}}^2 + \mathcal{K}_{\mathbf{k},+}^{jl})^2 t_{\perp}^2 \mathcal{K}_{\mathbf{k},-}^{jl}}{(\epsilon_{\mathbf{k}}^2 + \mathcal{K}_{\mathbf{k},-}^{jl})(\epsilon_{\mathbf{k}}^2 - \mathcal{K}_{\mathbf{k},+}^{jl})^2 + (\epsilon_{\mathbf{k}}^2 + \mathcal{K}_{\mathbf{k},+}^{jl})^2 t_{\perp}^2 \mathcal{K}_{\mathbf{k},-}^{jl}}, \qquad (19)$$
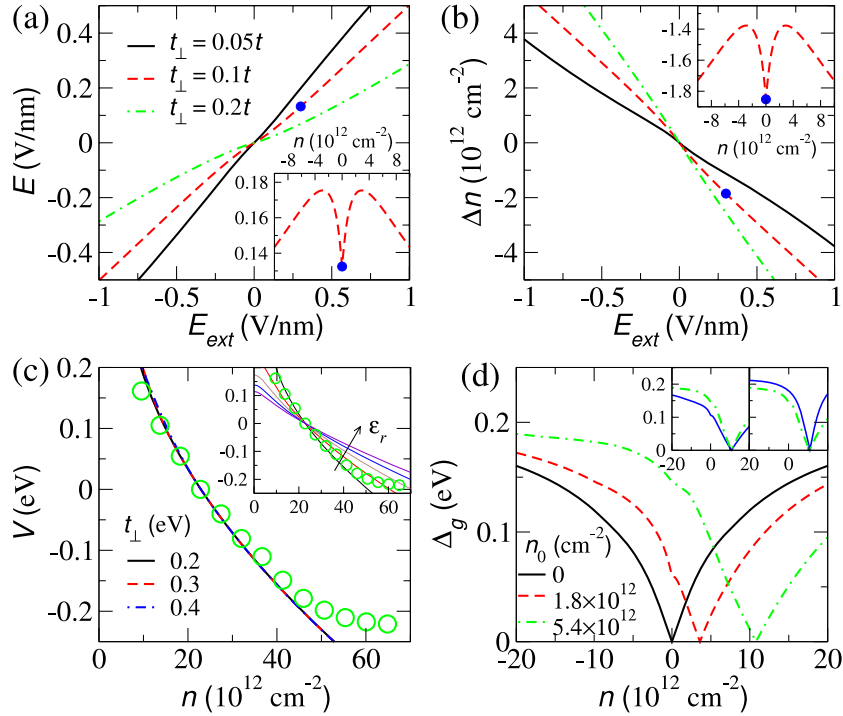
Figure 3. ((a), (b)) Respectively, screened electric field and charge imbalance versus E_{ext} at half-filling; the insets show the effect of changing n at fixed $E_{ext} = 0.3$ V nm^{-1}, signalled by the (blue) dot in the main panels. (c) V versus n for the BLG device shown in the right panel of figure 2(a): symbols are experimental data from [8]; lines are the result from (21) for $\varepsilon_r = 1$; the effect of changing $\varepsilon_r = 1 - 5$ is shown in the inset. (d) Gap versus n for the BLG device shown in the left panel of figure 2(a) with $t_\perp \simeq 0.22$ eV and $\varepsilon_r = 1$; the left inset compares the $n_0 = 5.4 \times 10^{12}$ cm^{-2} result for $\varepsilon_r = 1$ (green dashed–dotted) with $\varepsilon_r = 2$ (blue full line); the right inset shows the $n_0 = 5.4 \times 10^{12}$ cm^{-2} result for the screened V given by (20) (dashed–dotted line) and for the unscreened V given by (15) (full line). We used as the in-plane hopping $t \simeq 3$ eV.

where $\epsilon_{\mathbf{k}}$ is the SLG dispersion, and $\mathcal{K}_{\mathbf{k},\pm}^{jl} = (V/2 \pm E_{\mathbf{k}}^{jl})^2$ with $E_{\mathbf{k}}^{jl}$ given by (7). Taking the limit $N_c \to \infty$, it is possible to write (19) as an energy integral weighted by the density of states of SLG, as described in appendix A. What is important to note is that in order to calculate Δn we must specify V, which in turn depends on Δn through (17). Thus, a self-consistent procedure must be followed. In particular, for the two experimental realizations of biased BLG discussed in section 3.2.1, the self-consistent equation that determines V reads: in the case of exfoliated BLG [10],

$$V = \left[\frac{n}{n_0} - 2 + \frac{\Delta n(n, V)}{n_0}\right]\frac{e^2 n_0 d}{2\varepsilon_r \varepsilon_0};\qquad(20)$$

in the case of epitaxial BLG [8],

$$V = \left[2 - \frac{n}{n_a} + \frac{\Delta n(n, V)}{n_a}\right]\frac{e^2 n_a d}{2\varepsilon_r \varepsilon_0}.\qquad(21)$$

The self-consistent electric field $E = E_{ext} + E_{int}$ in the BLG region, with E_{int} given by (17) for $\varepsilon_r = 1$, is shown at half-filling as a function of E_{ext} in figure 3(a). The screened E is approximately a linear function of E_{ext}, with a constant of proportionality that depends on the specific value of $t_\perp$. Increasing $t_\perp$ leads to an increased screening, which can be understood as due to an increased charge imbalance between layers, as shown in figure 3(b). The highly non-linear effect

of inducing a finite carrier density ($n \neq 0$) can be seen in the insets of figures 3(a) and (b), for $t_\perp = 0.1t$ and $E_{ext} = 0.3$ V nm^{-1}.

As a validation test of the present self-consistent treatment, we compare (21) with experimental results for V obtained by fitting ARPES measurements from [8], as mentioned in section 3.2.1. The result is shown in figure 3(c). Clearly, the self-consistent V given by (21) for $\varepsilon_r = 1$ is a much better approximation than the unscreened result of (16) (see figure 2(c)). The best fit is obtained for $\varepsilon_r \sim 1$–2, as can be seen in the inset of figure 3(c). The value $\varepsilon_r \approx (\varepsilon_{SiC}+1)/2 \approx 5$ is too high, possibly because the bottom capacitor plate is, indeed, due to interface states, and therefore is not buried inside the SiC substrate [61, 62, 65]. Note, however, that the dielectric constant ε_r may effectively be tuned externally, as recently shown for SLG by adding a water overlayer in an ultra-high vacuum [68]. In figure 3(d) we show the gap Δ_g as a function of the carrier density n for the biased BLG device shown in the left panel of figure 2(a), with realistic values of the chemical doping n_0 [10]. The gap is given by (11), with $t_\perp \simeq 0.22$ eV [10] and V obtained by solving self-consistently (20) for $\varepsilon_r = 1$. Note that for $E_{ext} = 0$ we always have $E_{int} = 0$ (the charge imbalance must be externally induced), and therefore we also have $V = 0$ and $\Delta_g = 0$. For this particular biased BLG device the present model predicts $E_{ext} = 0$ for $n = 2n_0$, which explains the asymmetry for Δ_g versus n shown in figure 3(d).
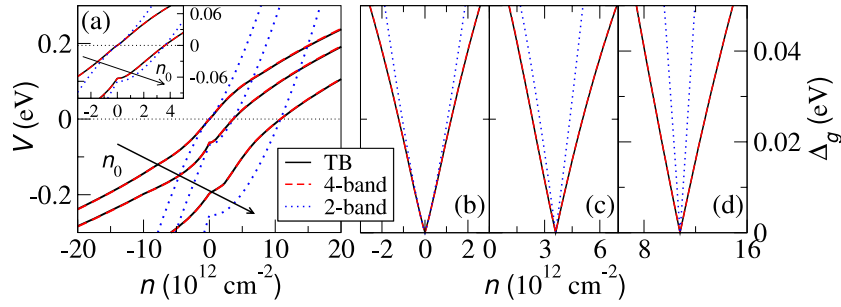
Figure 4. (a) Screened V versus n for the BLG system shown in the left panel of figure 2(a) computed within three different approaches (see the text): full tight-binding (TB), the four-band approximation, and the two-band approximation. Three different chemical dopings have been considered, $n_0 = \{0, 1.8, 5.4\} \times 10^{12}$ cm^{-2}. The inset shows a zoom around $V = 0$ for $n_0 = \{0, 1.8\} \times 10^{12}$ cm^{-2}. ((b)–(d)) Screened gap versus n obtained using V shown in (a) for $n_0 = \{0, 1.8, 5.4\} \times 10^{12}$ cm^{-2}, respectively. Parameters: $t \simeq 3$ eV, $t_\perp \simeq 0.22$ eV, and $\varepsilon_r = 1$.

The most important characteristic of such devices, from the point of view of applications, is the maximum size of the gap which could be induced. The maximum Δ_g occurs when V_g reaches its maximum, which occurs just before the breakdown of SiO$_2$. The breakdown field for SiO$_2$ is $\gtrsim 1$ V nm^{-1}, meaning that V_g values as high as 300 V are possible for the device shown in the left panel of figure 2(a). From (14) we see that $V_g \simeq \pm 300$ V implies $n - n_0 \simeq \pm 22 \times 10^{12}$ cm^{-2}, and therefore figure 3(d) nearly spans the interval of possible densities. It is apparent, especially for $n_0 = 5.4 \times 10^{12}$ cm^{-2}, that when the maximum allowed densities are reached the gap seems to be approaching a saturation limit. This saturation is easily identified with the plateau shown in figure 1(b) for Δ_g versus V, occurring for $V \gtrsim t_\perp$. We may then conclude that such devices enable the entire range of allowed gaps (up to $t_\perp$) to be accessed—as has been shown in very recent experiments [16, 17]. The effect of using a different dielectric constant ($\varepsilon_r = 2$) is shown as a full line in the left inset of figure 3(d), and the result for the unscreened case in the right inset, both for $n_0 = 5.4 \times 10^{12}$ cm^{-2}. The former makes the gap slightly smaller, and the latter slightly larger, but the main conclusions remain.

3.2.3. Screening in continuum models. The self-consistent Hartree approach considered in the previous section has been applied to the full tight-binding Hamiltonian given in (1). Here we compare the results for the potential difference V and gap Δ_g when the screening correction is used within the continuum approximation, either for the four-band model (5) or for the two-band model (6). This self-consistent Hartree approach in the continuum has been followed in [27, 12].

In the case of the four-band model, Δn is still given by (19) with the substitutions $\epsilon_k \rightarrow v_F p$ and $\frac{2}{N_c A_\bigcirc} \sum_{j,l=\pm} \sum'_k \rightarrow \frac{2}{\pi \hbar^2} \sum'_{j,l=\pm} \int_{p_1}^{p_2} dp\, p$, where the prime on the right-hand summation means a sum over total or partially occupied bands. Depending on the band in question and the value of the Fermi energy E_F, the limits of integration are $p_1, p_2 = \{0, p^\pm, \Lambda\}$, where

$$v_F p^\pm = \sqrt{E_F^2 + V^2/4 \pm \sqrt{E_F^2(V^2 + t_\perp^2) - t_\perp^2 V^2/4}}, \quad (22)$$

and Λ is a BZ cut-off that can be chosen such that $\frac{4\pi}{\hbar^2} \int_0^\Lambda dp\, p = \frac{4\pi^2}{A_\bigcirc} \Leftrightarrow \Lambda = \hbar\sqrt{\pi/A_\bigcirc}$. As regards the gap Δ_g, in the four-band model it is still given by (11).

For the two-band model case, the charge imbalance can be written as an integral in momentum space of the function $|\phi_{B1}|^2 - |\phi_{A2}|^2 = \pm V/(V^2 + 4v_F^4 p^4/t_\perp^2)^{1/2}$, where $\Phi = (\phi_{B1}, \phi_{A2})$ is the two-component wavefunction obtained by diagonalizing (6). The $\pm$ signs stand for the contribution of valence and conduction bands, respectively. In particular, at half-filling the charge imbalance is given by

$$\Delta n_{1/2} \simeq -\frac{t_\perp V}{2\pi v_F^2 \hbar^2} \ln\left(2t_\perp/|V| + \sqrt{4t_\perp^2/V^2 + 1}\right), \quad (23)$$

where we have included a factor of 4 to account for both spin and valley degeneracies. The BZ cut-off Λ has been chosen such that $v_F \Lambda = t_\perp$ [12]. Since in the two-band model it is assumed that $V \ll t_\perp$ holds we can write $\Delta_{1/2} \approx -t_\perp V/(2\pi v_F^2 \hbar^2) \ln(4t_\perp/|V|)$, which, from (17), leads to the logarithmic divergence of the screening ratio at small external electric field, $E_{ext}/E \sim -\ln E$, as mentioned in [13]. For a general filling n the charge imbalance reads

$$\Delta n \approx \frac{t_\perp V}{2\pi v_F^2 \hbar^2} \ln\left(\frac{v_F^2 \hbar^2 \pi |n|}{2t_\perp^2} + \sqrt{\frac{v_F^4 \hbar^4 \pi^2 n^2}{4t_\perp^4} + 1}\right), \quad (24)$$

where the charge density is given in terms of the Fermi wavevector as $n = \pm p_F^2/(\pi \hbar^2)$. Inserting (24) into (20) or (21) we get the expression for V in the two-band approximation, which is exactly the gap in the two-band model, $\Delta_g = |V|$.

In figure 4(a) the electrostatic energy difference between planes obtained, V, is shown for the three different approaches discussed above. The full (black) lines stand for the full tight-binding result, with V given by (20) and the charge imbalance Δn by (19). The result obtained in the four-band approximation is shown as dashed (red) lines. It can hardly be distinguished from the full tight-binding result, even when the chemical doping n_0 is as high as 5.4×10^{12} cm^{-2} (see the figure caption). In fact, the only prerequisite for the continuum four-band approximation (5) to hold is that $|E_F| \ll t$, which is always realized for the available BLG devices. As regards the two-band approximation model, we show as dotted (blue) lines the self-consistent result for V, obtained

for Δn as in (24). Clearly, it is only when both the bilayer density n and the chemical doping n_0 are small enough for the relation $|E_F|, V \ll t_\perp$ to hold that the two-band model is a good approximation (see the inset). The same conclusions apply to the behaviour of the gap Δ_g as a function of the carrier density n, which is shown in panels 4(b)–(d) for $n_0 = \{0, 1.8, 5.4\} \times 10^{12} \text{ cm}^{-2}$, respectively. The failure of the two-band model in the presence of interactions was also observed in Hartree calculations of the electron compressibility [69].

3.2.4. Electron–hole asymmetry. As we have seen in sections 3.2.1 and 3.2.2, the two biased BLG devices shown in figure 2(a) have zero gap when the carrier density is twice the system's chemical doping. The closing of the gap at a finite density induces an electron–hole asymmetric behaviour in the system, where obvious examples are the gap Δ_g and the electrostatic energy difference between layers V, as shown in figures 2(d) and 4(a). An experimental confirmation for this electron–hole asymmetric behaviour comes from measurements of the cyclotron mass in the biased BLG device shown in the left panel of figure 2(a) [10] (discussed in more detail in section 4.1). However, real electron–hole asymmetry can also be present in BLG due to extra hopping terms, as mentioned in section 2. Here we study how Δ_g and V are affected by the electron–hole symmetry breaking terms t', γ_4, and Δ, taking into account the screening correction.

Inclusion of in-plane second-NN hopping t' leads to a generalized version of (4), which can be written as $H_{\mathbf{k},t'} = H_{\mathbf{k}} - (\epsilon_{\mathbf{k}}^2 t'/t - 3t')\mathbf{1}$, where $H_{\mathbf{k}}$ is given by (4), $\epsilon_{\mathbf{k}}$ is the SLG dispersion, and $\mathbf{1}$ is the 4×4 identity matrix. The generalized BLG dispersion, either biased or unbiased, is given by the $t' = 0$ result added by $-\epsilon_{\mathbf{k}}^2 t'/t + 3t'$, which clearly breaks electron–hole symmetry. Note that a finite t' has no influence on the wavefunction amplitude. Therefore, the integrand in (18)—the definition of the charge carrier imbalance between layers Δn—is independent of t'. We have found numerically, using a four-band continuum model, that neither the screened V nor the gap Δ_g is affected by t', although the gap becomes indirect for finite t'. This means that the structure of occupied $\mathbf{k}$s is insensitive to t', and thus Δn in (18) is fully t' independent, at least as long as $E_F \ll t$. Even though the presence of t' can lead to the suppression of the Mexican hat in the valence band, this only happens for $|V| < t_\perp^2 t' \sim 10^{-3} t$. For such a small $|V|$ value the Mexican hat plays an irrelevant role. The band structure around the K point for $t' = 0.1t$ (solid line) and $t' = 0$ (dashed line) can be seen in figure 5(a) for typical parameter values.

Now we turn to the effect of the inter-layer second-NN hopping γ_4. The generalized version of (4) for finite γ_4, which we call $H_{\mathbf{k},\gamma_4}$, can be obtained by replacing the null entries (A1, A2) and ($B1$, $B2$) by $\gamma_4 s_{\mathbf{k}}^*$ and (A2, A1) and (B2, B1) by $\gamma_4 s_{\mathbf{k}}$. The associated eigenproblem admits an analytic treatment at low energies and small biases $v_F p, V \ll t_\perp$ [52], but as has been seen previously, $V \sim t_\perp$ is possible in real systems. Therefore, we analyse the problem numerically using a four-band continuum approximation. The matrix Hamiltonian $H_{\mathbf{k},\gamma_4}$ may then be written as $H_{\mathbf{k},\gamma_4} = M^\dagger \tilde{H}_{\mathbf{k},\gamma_4} M$ near the K points, with $M = \text{diag}[1, e^{i\varphi_{\mathbf{p}}}, e^{-i\varphi_{\mathbf{p}}}, 1]$, and $\tilde{H}_{\mathbf{k},\gamma_4}$ obtained from (5)
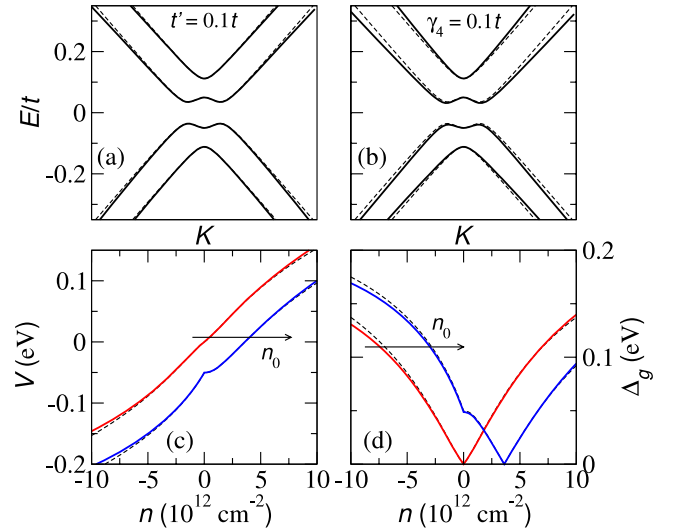

Figure 5. ((a), (b)) Band structure around K for the biased BLG with $t' = 0.1t$ and $\gamma_4 = 0.1t$, respectively, for $V = t_\perp = 0.1t$. Dashed lines: $t' = \gamma_4 = 0$. ((c), (d)) Respectively, V versus n and Δ_g versus n for the BLG device shown in the left panel of figure 2(a), modelled with a finite γ_4. Parameters: $t \simeq 3$ eV, $t_\perp = 0.1t$, $\gamma_4 = 0.1t$, $\varepsilon_r = 1$, and $n_0 = \{0, 1.8\} \times 10^{12} \text{ cm}^{-2}$. Dashed lines: $t' = \gamma_4 = 0$.

with $\varphi_{\mathbf{p}} = 0$ and the null entries (A1, A2), (B1, B2), (A2, A1), and (B2, B1) replaced by $-v_4 p$, where $v_4 = \gamma_4 a\hbar^{-1}\sqrt{3}/2 \lesssim 10^5 \text{ m s}^{-1}$. The canonical transformation defined by M clearly shows that the problem still has cylindrical symmetry in the continuum approximation. Around the K' points we have $H_{K',\gamma_4} = M \tilde{H}_{K,\gamma_4} M^\dagger$. The band structure obtained for $\gamma_4 = 0.1t$ (solid lines) and $\gamma_4 = 0$ (dashed lines) is shown in figure 5(b) for typical parameter values. Note that, even though the gap becomes indirect for $\gamma_4 \neq 0$, we still have $E_{p=0} = \{\pm V/2, \pm\sqrt{t_\perp^2 + V^2/4}\}$ as in the $\gamma_4 = 0$ case. The screened electrostatic energy difference between layers V for the biased BLG device shown in the left panel of figure 2(a) is shown as a function of the carrier density in figure 5(c). The result for V has been obtained by solving (20) with carrier imbalance Δn given by the continuum version of (18), with wavefunctions obtained numerically through $\tilde{H}_{K,\gamma_4}$ for $\gamma_4 = 0.1t$ (see the figure caption for other parameter values). The corresponding screened gap Δ_g is shown in panel 5(d). The $\gamma_4 = 0$ result is also shown as a dashed line for both V and Δ_g. The effect of γ_4 may clearly be considered small, even for such a large value as $\gamma_4 \simeq 0.3$ eV. However, electronic properties which are particularly sensitive to the changes of the Fermi surface (for instance, the cyclotron mass) may, in principle, be measurably affected by γ_4. We will come back to this point in section 4.1.

As regards the on-site energy Δ, since it is smaller than γ_4 (see section 2) we consider their simultaneous effect. The additional term in the Hamiltonian adds to the matrix $H_{\mathbf{k},\gamma_4}$ the contribution $\text{diag}[\Delta, 0, 0, \Delta]$, and therefore the four-band continuum approximation for finite γ_4 and Δ may be written as $\tilde{H}_{K,\gamma_4,\Delta} = \tilde{H}_{K,\gamma_4} + \text{diag}[\Delta, 0, 0, \Delta]$, where we use the same transformation M as was introduced above. Similarly to the γ_4 case, the effect of Δ is negligible for both V and Δ_g.

3.3. The DOS and LDOS

Insight into the electronic properties of biased (and unbiased) BLG can also be achieved by studying the density of states (DOS) and the local DOS (LDOS) of the system. In particular, the LDOS can be accessed through scanning tunnelling microscopy/spectroscopy measurements [70], providing a useful way to validate theoretical models. On the other hand, the knowledge of the DOS turns out to be very useful for practical purposes, as it provides a way to relate the Fermi energy E_F and the carrier density n in the system: $|n| = \int_0^{|E_F|} dE\, \rho_2(E)$, where $\rho_2(E)$ stands for the BLG DOS.

We have computed the analytical expression for the DOS of BLG, valid over the entire energy spectrum and for zero and finite bias. The expression is given in appendix B. As regards the LDOS, the results have been obtained using the recursive Green's function method [71]. The DOS and LDOS of unbiased BLG have been obtained previously within the effective mass approximation in [72]. The effect of disorder on the DOS and LDOS of BLG, both biased and unbiased, has also been studied recently [18, 29, 30, 72, 73, 31].

The DOS (full line) and LDOS (dashed and dash–dotted lines) for the biased BLG are shown in figures 6(a) and (b) for $V = 0.05t$. The asymmetry among the four sublattices is evident, in particular between sites B1 and A2, and between A1 and B2, which are equivalent in the unbiased system. Note that close to the gap edges the states corresponding to positive energies have a larger amplitude at B1 sites, while those corresponding to negative energies have a larger amplitude at A2 sites. This behaviour agrees with the observation that B1 and A2 are the low energy active sites (the basis for the two-band model), and it also reflects our choice of electrostatic energies in (3): $+V/2$ in layer 1 and $-V/2$ in layer 2. The asymmetry between B1 and A2 sites can be understood with the two-band continuum model, valid for $v_F p, V \ll t_\perp$. Defining the LDOS as $\rho_{B1/A2}(E) = \frac{1}{N_c} \sum_{\mathbf{k}} |\phi_{B1/A2,\mathbf{k}}|^2 \delta(E - E_{\mathbf{k}})$, where $\Phi_{\mathbf{k}} = (\phi_{B1,\mathbf{k}}, \phi_{A2,\mathbf{k}})$ is the two-component wavefunction obtained by diagonalizing (6), we can readily arrive at the following expressions:

$$\rho_{B1/A2}(E) = \frac{1}{2\sqrt{3}\pi} \frac{t_\perp}{t^2} \mathrm{sgn}(E) \frac{E \pm V/2}{\sqrt{E^2 - V^2/4}}. \qquad (25)$$

The asymmetric behaviour is apparent, with $\rho_{B1}(E)$ diverging for $E \to V/2^+$ and $\rho_{A2}(E)$ for $E \to -V/2^-$. The result for $\rho_{A2}(E)$ is shown in figure 6(c) for $V \simeq \{0.87, 4.23, 7.87\} \times 10^{-3}t$ and $t_\perp = 0.1t$. Within the screening corrected parallel plate capacitor model discussed in section 3.2, these V values correspond to carrier densities $n \simeq \{0.2, 0.8, 1.4\} \times 10^{12}\,\mathrm{cm}^{-2}$, respectively, where we have used $t \simeq 3.1$ eV, $n_0 = 0$, and $\varepsilon_r = 1$. The full lines are the recursive Green's function method [71] results and dashed lines are the results of (25). As expected, the closer to the gap edges, the better the agreement between the two approaches.

A strong suppression of electrical noise in BLG has been reported recently by Lin and Avouris [74]. For devices made from exfoliated BLG on top of SiO_2, the current fluctuations are thought to originate from the fluctuating trapped charges in the oxide. Therefore, the more effective the impurity charge
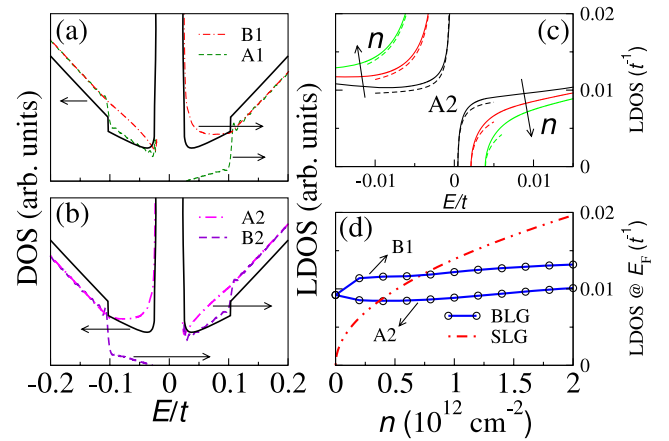

Figure 6. ((a), (b)) LDOS of BLG at A1/B1 and A2/B2 sites, respectively, for $V = 0.05t$ and $t_\perp = 0.1t$. The total DOS is shown as a full line. (c) LDOS at A2 sites for $n \simeq \{0.2, 0.8, 1.4\} \times 10^{12}\,\mathrm{cm}^{-2}$ and $t_\perp = 0.1t$. Full lines stand for numerical results and dashed lines for (25). (d) LDOS at E_F versus n for BLG and SLG.

screening in the system, the lower the electrical noise. Having lower noise in BLG than in SLG may then be attributed to the low energy finite DOS in the former. However, it has also been reported in [74] that while increasing the carrier density in SLG leads to lower noise, as expected due to the more effective impurity screening, it results in higher noise in BLG. Insight into this behaviour is achieved by analysing the LDOS at the Fermi level E_F in a biased BLG, as charging the system through the back gate V_g leads to a finite perpendicular electric field. In figure 6(e) we show the biased BLG LDOS at E_F for B1 and A2 sites as a function of carrier density n in the system. For a given n, the electrostatic energy difference V is evaluated self-consistently through (20), with $n_0 = 0$ and $\varepsilon_r = 1$, and E_F is obtained by integrating over the DOS. Additionally, we use $t \simeq 3$ eV and $t_\perp = 0.1t$. We have chosen densities in the range $n \in [0 - 2] \times 10^{12}\,\mathrm{cm}^{-2}$, which corresponds to back gate voltages $V_g \in [0-27]$ eV through (14), which is similar to the experimental range in [74]. The main observation to be made as regards the results of figure 6(e) is that for the low energy active sublattices B1 and A2 the LDOS at E_F remains approximately constant with increasing electron density, as opposed to the $\sim\sqrt{n}$ dependence found in SLG. This is an indication that impurity screening may not be increasing with carrier density in the biased BLG system, which may be contributing to enhanced electrical noise.

4. Magnetic field effects

In the biased BLG system, as a consequence of the gapped band structure discussed in section 3, a perpendicular magnetic field is expected to induce distinct features in electronic properties. In this section we focus on the cyclotron mass (semi-classical approach) and on the cyclotron resonance (quantum regime) comparing the theory with experimental results.

4.1. The cyclotron mass

In the semi-classical approximation the cyclotron effective mass m_c is given by

$$m_c = \frac{\hbar^2}{2\pi} \frac{\partial A(E)}{\partial E}\bigg|_{E=E_F}, \tag{26}$$

where $A(E)$ is the k-space area enclosed by the orbit of energy E, and the derivative is evaluated at the Fermi energy E_F [75–77]. It can be accessed experimentally through the Shubnikov–de Haas effect, providing a direct probe to the Fermi surface. In the case of exfoliated graphene, either SLG or (un)biased BLG, the Fermi energy can be varied by tuning the back gate voltage, and therefore a significant portion of the whole band structure may be unveiled. In particular for the biased BLG, the presence of a finite gap can be checked and the model developed in section 3 tested.

4.1.1. Comparison with experiment.
General expressions for m_c obtained for the full tight-binding bands (7), valid for the relevant parameter range $V \lesssim t_\perp \ll t$ and restricted to $E_F < t$, are given in appendix C. In figure 7(a) we compare the theory results for the cyclotron mass with experimental measurements on the biased BLG system shown in the left panel of figure 2(a). We have only considered m_c associated with low energy bands $E_\mathbf{k}^{\pm-}$ (see (7)), since $E_\mathbf{k}^{\pm+}$ are inactive for the experimentally available carrier densities. The dashed lines stand for the unscreened result, where V is given by (15), and the solid lines are the screened result, with V given by (20). The inter-layer coupling $t_\perp$ has been taken as an adjustable parameter, keeping all others fixed: $t \simeq 3$ eV, $\varepsilon_r = 1$, and $n_0 = 1.8 \times 10^{12}$ cm^{-2}. The value of $t_\perp$ could then be chosen such that theory and experiment gave the same m_c for $n = 2n_0 \approx 3.6 \times 10^{12}$ cm^{-2}. As discussed in section 3.2.2, at this particular density the gap closes, meaning that the theoretical value becomes independent of the screening assumptions. We found $t_\perp \approx 0.22$ eV, in good agreement with values found in the literature. The theoretical dependence $m_c(n)$ agrees well with the experimental data for the case of electron doping. Also, as seen in figure 7(a), the screened result provides a somewhat better fit than the unscreened model, especially at low electron densities. This fact, along with the good agreement found for the electrostatic energy difference data of [8] (see figure 3(c)), allows us to conclude that for doping of the same sign from both sides of bilayer graphene, the gap is well described by the screened approach. In the hole doping region in figure 7(a), the Hartree approach underestimates the value of m_c whereas the simple unscreened result overestimates it. This can be attributed to the fact that the Hartree theory used here is reliable only if the gap is small compared to $t_\perp$. In the experimental realization of [10], $n_0 > 0$ and, therefore, the theory works well for a wide range of electron doping $n > 0$, whereas even a modest overall hole doping $n < 0$ corresponds to a significant electrostatic difference between the two graphene layers. In this case, the unscreened theory overestimates the gap whereas the Hartree calculation underestimates it.

In figure 7(b) we compare our best fit to the cyclotron mass (full line) with results obtained for different parameter
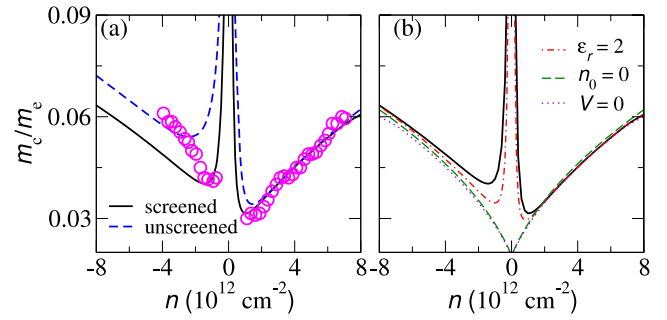

Figure 7. Cyclotron mass versus n, normalized to the free electron mass, m_e. (a) Solid lines are the result of the self-consistent procedure and the dashed lines correspond to the unscreened case; $t \simeq 3$ eV, $t_\perp \simeq 0.22$ eV, $\varepsilon_r = 1$, and $n_0 = 1.8 \times 10^{12}$ cm^{-2}. Circles are experimental data from [10]. (b) The screened result in (a) is compared with the result for $\varepsilon_r = 2$, the case without chemical doping ($n_0 = 0$), and the case where the external field is zero ($V = 0$).

values. The dashed–dotted lines stand for m_c obtained with $\varepsilon_r = 2$ in (20). As can be seen clearly, the $n > 0$ result is not substantially affected, while for $n < 0$ the theory description of m_c worsens. This is due to the reduction of the gap when ε_r is increased (see the left inset in figure 3(d)). The dashed lines in figure 7(b) are obtained with $n_0 = 0$, where the zero gap occurs at the neutrality point. The dotted lines are the result for $E_{\text{ext}} = 0 = V$, i.e., zero gap at every density value. Note that these two results, $n_0 = 0$ and $V = 0$, show an electron–hole symmetric m_c, contradicting the experimental result. It may then be said that the electron–hole asymmetry observed in m_c is a clear indication of the presence of a finite gap in the spectrum. It will be shown in section 4.1.3 that, if we ignore the gap, this electron–hole asymmetry cannot be described by taken into account t', γ_4 or Δ.

4.1.2. The cyclotron mass in continuum models.
Here we compare our results for the cyclotron mass, which has been obtained with expressions shown in appendix C, with the results of continuum models.

Within the four-band continuum model given by (5), where the dispersion is just the full tight-binding result (7) with the substitution $\epsilon_\mathbf{k} \to v_F p$, we can easily derive the following analytical expression for m_c:

$$m_c = \frac{E_F}{v_F^2} \left[1 + \frac{V^2 + t_\perp^2}{2\sqrt{E_F^2(V^2 + t_\perp^2) - t_\perp^2 V^2/4}} \right]. \tag{27}$$

In figure 8(a) the dashed line is the result of (27), where V has been computed self-consistently using (20) and the four-band continuum approximation discussed in section 3.2.3. As expected, the agreement with the full tight-binding result (shown as a full line) is excellent for the densities considered. Note that there is an extra solution given by $\tilde{m}_c v_F^2 = E_F[1 - (V^2 + t_\perp^2)/\sqrt{4E_F^2(V^2 + t_\perp^2) - t_\perp^2 V^2}]$, valid when $|E_F| < V/2$ or $|E_F| > \sqrt{V^2/4 + t_\perp^2}$, which corresponds to the extra orbit appearing when E_F falls in the Mexican hat region, or
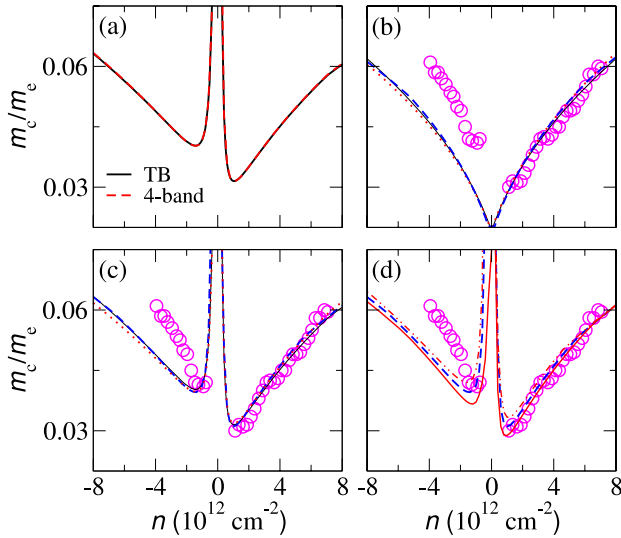
Figure 8. Cyclotron mass versus n, normalized to the free electron mass, m_e. (a) Comparison between full tight-binding (TB) and four-band approximation, for $t_\perp \simeq 0.22$ eV and $n_0 = 1.8 \times 10^{12}$ cm^{-2}. ((b), (c)) Effect of finite t' and γ_4 for $n_0 = 0$ (b) and $n_0 = 1.8 \times 10^{12}$ cm^{-2} (c): the dotted line is for $t' \simeq 0.3$ eV and $t_\perp \simeq 0.22$ eV; the dashed line is for $\gamma_4 \simeq 0.12$ eV and $t_\perp \simeq 0.19$ eV; the full thin line is for $t' = \gamma_4 = 0$ and $t_\perp = 0.22$ eV. (d) Effect of Δ for $\gamma_4 \simeq 0.12$ eV and $t_\perp \simeq 0.19$ eV: the full line is for $\Delta \simeq 0.03$ eV; the dotted–dashed line is for $\Delta \simeq -0.03$ eV; the dashed line is for $\Delta = 0$. Circles are experimental data from [10]. We have used $t \simeq 3$ eV and $\varepsilon_r = 1$.

above the bottom of high energy bands. We can estimate the densities for which these two regions start playing a role: using $V \sim 0.1t_\perp \sim 0.01t$ in the Mexican hat region (valid for $n_0 \lesssim 2 \times 10^{12}$ cm^{-2}) we get $n \lesssim 10^{11}$ cm^{-2}; setting $V \sim t_\perp \sim 0.1t$ around the bottom of high energy bands we get $n \gtrsim 10^{13}$ cm^{-2}. These two density values are outside the range of experimentally realized densities (see figure 7(a)).

4.1.3. The effect of electron–hole asymmetry. In section 3.2.4 the effect of electron–hole symmetry breaking parameters— namely, t', γ_4, and Δ—has been studied as regards the self-consistent description of the gap. Here we extend the analysis to the cyclotron mass, restricting ourselves to the biased BLG device shown in the left panel of figure 2(a). Results have been obtained within the four-band model. As all cases have cylindrical symmetry around K and K′, the cyclotron mass may be written as $m_c = p_F/(\partial E_F/\partial p_F)$.

In figure 8(b) we show the m_c result for finite t' (dotted red line) and finite γ_4 (dashed blue line), keeping $n_0 = 0$ (the absence of electron–hole asymmetry due to chemical doping). The thin full line is the result obtained for $t' = \gamma_4 = 0$ in section 4.1.1, and circles are experimental data from [10]. The $n > 0$ region, where the smaller gaps are realized experimentally, is still well fitted if we choose $t_\perp \simeq 0.22$ eV with $t' \simeq 0.3$ eV or $t_\perp \simeq 0.19$ eV with $\gamma_4 = 0.12$ eV (we use $t \simeq 3$ eV). However, it is clear that neither of these results can account for the electron–hole asymmetry observed experimentally. In fact, a closer look reveals that m_c for finite t' have the opposite trend, being smaller than the $t' = 0$ result

for $n < 0$ and larger for $n > 0$, as would be expected by inspection of the energy bands in figure 5(a). Such an opposite trend should also be seen for finite γ_4, although the effect is not as large as expected from the considerable distortion of the energy bands shown in figure 5(b). This attenuation can be understood as the result of fixing the carrier density n and not the Fermi energy E_F: changing γ_4 (or t') for a given n leads to a different E_F, and the new E_F is such that it counteracts the expected effect of γ_4 (or t') in m_c. Figure 8(c) shows the same as (b) for $n_0 = 1.8 \times 10^{12}$ cm^{-2}. The effect of the on-site energy Δ is shown in figure 8(d) for fixed $\gamma_4 \simeq 0.12$ eV, $t_\perp \simeq 0.19$ eV and $n_0 = 1.8 \times 10^{12}$ cm^{-2}. The result for $\Delta = 0$ (dashed line) is shown along with the results for $\Delta \simeq 0.03$ eV (full line) and $\Delta \simeq -0.03$ eV (dotted–dashed line). It is clear that the effects of t', γ_4 and Δ on the cyclotron mass can be neglected.

4.2. Cyclotron resonance

The effect of a perpendicular magnetic field can be studied within the continuum approximation through minimal coupling $\mathbf{p} \to \mathbf{p} - e\mathbf{A}$ [7]. The case of biased BLG has been studied within both the four-band (5) and two-band (6) continuum models in [12, 11, 36, 78]. Here we use the same approach to study the cyclotron resonance (i.e. the Landau level transition energies) with the extra ingredient that the parameter V depends on the filling factor, as discussed in section 3.2.

In the four-band model standard manipulations [7, 11, 36, 79] lead to the unbiased BLG Landau level spectrum

$$E_n^{\pm\pm} = \pm\sqrt{(1+2n)\frac{\gamma^2}{2} + \frac{t_\perp^2}{2} \pm \sqrt{(\gamma^2 + t_\perp^2)^2/4 + n\gamma^2 t_\perp^2}}, \tag{28}$$

where $\gamma = \sqrt{2}v_F\hbar/l_B$, with $l_B = \sqrt{\hbar/|e|B}$ for the magnetic length. Non-zero ($n \geqslant 1$) eigenenergies are fourfold degenerate due to valley and spin degeneracy, while zero-energy Landau levels have eightfold degeneracy, since there are two zero-energy Landau states ($n = -1, 0$) per valley per spin. The two-band model result $E_n^{\pm} \approx \pm\gamma^2 t_\perp^{-1}\sqrt{n(n+1)}$ is easily recovered from (28) for $\gamma \ll t_\perp$, being valid for magnetic fields up to $B \approx 1$ T [7].

The Landau level transition energies in BLG have been recently obtained through cyclotron resonance measurements [80]. The data were found to deviate from what would be expected through (28), especially for larger filling factors. It should be noted, however, that in order to keep a constant filling factor and vary the magnetic field, as was done in [80], the back gate voltage V_g has to be tuned to compensate for the variation of the Landau level degeneracy. As we have seen previously, tuning V_g is equivalent to changing V—the electrostatic energy difference between layers—which means that (28) is no longer valid, as recently shown within the four-band continuum model [36]. To have an estimate for the effect of the back gate voltage on the Landau level spacing we have computed Landau level energy differences, taking into account the variation of V with carrier density n. We have used the unscreened result given by (15), with $n_0 = 0$ and $\varepsilon_r = 1$. Within this approximation we can easily write V in terms of the

filling factor ν and magnetic field B as $V = \nu B e^2 d/(2\varepsilon_0 \phi_0) \approx 7.4 \times 10^{-4} \nu B$, with B in teslas in the last step. Thus, for fixed filling factor, V varies linearly with B. Note that the comparison between this unscreened treatment of the biased BLG and the unbiased result (28) should give lower and upper limits for the effect of the perpendicular external field in the cyclotron frequency. In figure 9 we show the Landau transition energies obtained versus magnetic field for the given filling factors. The dashed lines represent the unbiased BLG result, as given by (28). The lines with crosses are the results for the unscreened biased BLG, and filled symbols are experimental data from [80]: circles for $\nu > 0$ and squares for $\nu < 0$. We have used $t = 3.5$ eV and $t_\perp = 0.1t$, consistent with [80]. As can be seen from figure 9, the back gate induced electric field gives rise to sizable effects already for magnetic fields and filling factors realized in experiments. Except at $\nu = \pm 8$, the result of (28) for the unbiased BLG and the unscreened biased BLG result effectively provide upper and lower limits on the experimental data. The observed electron–hole asymmetry could then be interpreted as due to an asymmetry in V versus n: larger V, and therefore larger gap, for $n < 0$; smaller V and gap for $n > 0$, which would make the result closer to the unbiased case. It should be noted that in such a case we would expect the neutrality point to occur for $V_g < 0$, as is the case for the NH_3 doped BLG studied before. For the system reported in [80], however, the opposite seems to be happening, as indicated by the Hall resistivity. A neutrality point for $V_g > 0$ is, in fact, the more usual effect of H_2O molecules adsorbed on graphene samples [56]. As a final remark regarding the results presented in figure 9, we note that the experimental data trend, which makes (28) a poor fit at $|\nu| \geqslant 8$, is still not accounted for in the biased BLG result. An alternative approach is the inclusion of the screening correction, which should go beyond (19), including the magnetic field effect. It has been reported recently that Dirac liquid renormalization may also be contributing to the observed trend [81].

5. Conclusions

We have studied the electronic behaviour of bilayer graphene in the presence of a perpendicular electric field—a *biased bilayer*—using the minimal tight-binding model that describes the system. The effect of the perpendicular electric field has been included through a parallel plate capacitor model, with screening correction at the Hartree level. We have compared the full tight-binding description with its four-band and two-band continuum approximations, and found that the four-band model is always a suitable approximation for the conditions realized in experiments. Also, we have studied the effect of electron–hole asymmetry terms and found that they have only a small effect on the electronic properties addressed here. The model has been applied to real biased bilayer devices, made out of either SiC [8] or exfoliated graphene [10, 9]. The good agreement with experimental results—namely, for the electrostatic energy difference between layers obtained through ARPES [8] and for the Shubnikov–de Haas cyclotron mass [10]—clearly indicates that the model is capturing the key ingredients, and that a finite gap is effectively being controlled
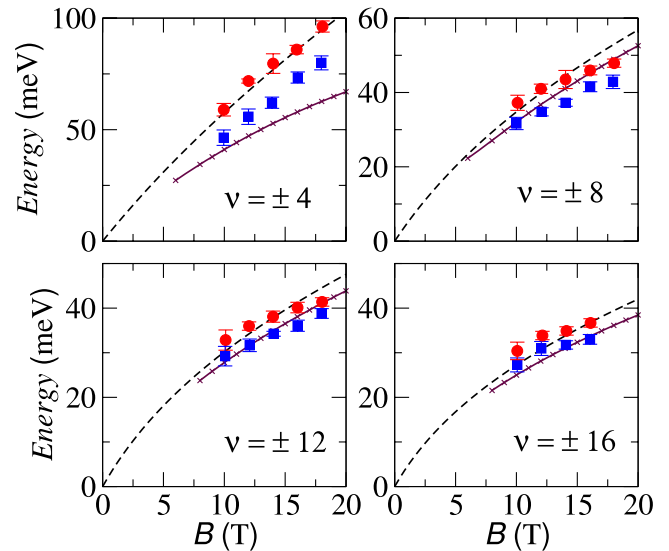
Figure 9. Landau level transition energies versus magnetic field for the given filling factors. The dashed line is the unbiased BLG result (28) and the line with crosses is the biased BLG result (see the text). We used $t = 3.5$ eV and $t_\perp = 0.1t$. Filled symbols are experimental data from [80]: circles for electrons and squares for holes.

externally. Analysis of recent experimental results as regards the electrical noise [74] and cyclotron resonance [80] further suggests that the model can be seen as a good starting point for understanding the electronic properties of graphene bilayers.

Acknowledgments

Appendix A. Asymmetry between layers

In order to write (19) as an energy integral, we start by introducing the SLG density of states per spin per unit cell defined for the conduction band as

$$\rho(\epsilon) = \frac{1}{N_c} \sum_{\mathbf{k}} \delta(\epsilon - t|s_{\mathbf{k}}|), \qquad (A.1)$$

with $s_{\mathbf{k}}$ as in (4). The momentum sum in (A.1) can be written as an integral by letting $N_c \to \infty$. The integration can be performed and written in terms of complete elliptic integrals of the first kind [5].

With the definition of $\rho(\epsilon)$ in (A.1) the charge imbalance between layers in (19) can be written as $\Delta n = \Delta n_{1/2} + \Delta \tilde{n}$, where the charge imbalance at half-filling $\Delta n_{1/2}$ is given by

$$\Delta n_{1/2} = \frac{2}{A_\circ} \sum_{l=\pm} \int_0^{3t} d\epsilon \, \rho(\epsilon) \mathcal{I}_{-l}(\epsilon), \qquad (A.2)$$

and the fluctuation $\Delta\tilde{n}$ with respect to the half-filled case is given by

$$\Delta\tilde{n} = \frac{2}{A_\bigcirc} \begin{cases} \sum_{l=\pm} \int_{\epsilon_1}^{\epsilon_2} d\epsilon\, \rho(\epsilon)\mathcal{I}_{+l}(\epsilon), & n > 0 \\ -\sum_{l=\pm} \int_{\epsilon_1}^{\epsilon_2} d\epsilon\, \rho(\epsilon)\mathcal{I}_{-l}(\epsilon), & n < 0, \end{cases} \quad (A.3)$$

where n is the carrier density with respect to half-filling. The integral kernel in (A.2) and (A.3) reads

$$\mathcal{I}_{jl}(\epsilon) = \frac{[\epsilon^2 + \mathcal{K}_-^{jl}(\epsilon)][\epsilon^2 - \mathcal{K}_+^{jl}(\epsilon)]^2 - [\epsilon^2 + \mathcal{K}_+^{jl}(\epsilon)]t_\perp^2 \mathcal{K}_-^{jl}(\epsilon)}{[\epsilon^2 + \mathcal{K}_-^{jl}(\epsilon)][\epsilon^2 - \mathcal{K}_+^{jl}(\epsilon)]^2 + [\epsilon^2 + \mathcal{K}_+^{jl}(\epsilon)]t_\perp^2 \mathcal{K}_-^{jl}(\epsilon)},$$
$$(A.4)$$

where $\mathcal{K}_\pm^{jl}(\epsilon) = [V/2 \pm E^{jl}(\epsilon)]^2$, with $E^{jl}(\epsilon)$ given by (7) with the substitution $\epsilon_\mathbf{k} \to \epsilon$. The limits of integration in (A.3) depend on the band label l and E_F as follows: with $l = -$ we have $\epsilon_1 = \epsilon^-$ and $\epsilon_2 = \epsilon^+$ for $E_F^2 < V^2/4$, while for $E_F^2 > V^2/4$ we have $\epsilon_1 = 0$ and $\epsilon_2 = \epsilon^+$; with $l = +$ we only have contribution for $E_F^2 > t_\perp^2 + V^2/4$, and the limits are $\epsilon_1 = 0$ and $\epsilon_2 = \epsilon^-$. We use the notation $\epsilon^\pm = [E_F^2 + V^2/4 \pm \sqrt{E_F^2(V^2 + t_\perp^2) - t_\perp^2 V^2/4}]^{\frac{1}{2}}$.

Appendix B. The bilayer DOS

The DOS per unit cell of BLG, either biased or unbiased, is defined as

$$\rho_2(E) = \frac{2}{N_c} \sum_\mathbf{k} [\delta(E - E_\mathbf{k}^{\pm-}) + \delta(E - E_\mathbf{k}^{\pm+})], \quad (B.1)$$

where $E_\mathbf{k}^{\pm\pm}$ is given by (7). Equation (B.1) can be written as a sum of two contributions, $\rho_2(E) = \sum_{l=\pm} \rho_2^l(E)$, where the label $l = \pm$ stands for contributions coming from bands $E_\mathbf{k}^{\pm l}$. For the experimentally relevant case where $\alpha = (V^4/4 + t_\perp^2 V^2/2)/(V^2 + t_\perp^2) < t^2$ the analytical expressions for each contribution read

$$\rho_2^-(E) = \frac{4}{t^2\pi^2}$$
$$\begin{cases} \psi^{--}(E)\mathcal{F}^-(E), & \Delta_g/2 < |E| < V/2 \\ \quad + \\ \psi^{-+}(E)\mathcal{F}^+(E), & \Delta_g/2 < |E| < E^{+-}(t) \\ \psi^{-+}(E)\mathcal{G}^+(E), & E^{+-}(t) < |E| < E^{+-}(3t) \end{cases} \quad (B.2)$$

and

$$\rho_2^+(E) = \frac{4}{t^2\pi^2} \begin{cases} \psi^{+-}(E)\mathcal{F}^-(E), & \\ \quad \sqrt{t_\perp^2 + V^2/4} < |E| < E^{++}(t) \\ \psi^{+-}(E)\mathcal{G}^-(E), & \\ \quad E^{++}(t) < |E| < E^{++}(3t), \end{cases}$$
$$(B.3)$$

with

$$\mathcal{F}^l(E) = \frac{\chi^l(E)}{\sqrt{F[\chi^l(E)/t]}} \mathbf{K}\left(\frac{4\chi^l(E)/t}{F[\chi^l(E)/t]}\right) \quad (B.4)$$

$$\mathcal{G}^l(E) = \frac{\chi^l(E)}{\sqrt{4\chi^l(E)/t}} \mathbf{K}\left(\frac{F[\chi^l(E)/t]}{4\chi^l(E)/t}\right), \quad (B.5)$$

and with $\psi^{\pm l}(E)$ given by

$$\psi^{\pm l}(E) = \frac{\mathcal{L}^l(E)\sqrt{\chi^l(E)^2 + t_\perp^2/2 + V^2/4 \pm \mathcal{L}^l(E)}}{\chi^l(E)|\mathcal{L}^l(E) \pm (t_\perp^2 + V^2)/2|}, \quad (B.6)$$

where $\mathcal{L}^l(E) = [t_\perp^4/4 + (t_\perp^2 + V^2)\chi^l(E)^2]^{1/2}$, and where $\chi^\pm(E)$ is as in the right-hand side of (22) with $E_F \to E$. We use $F(x) = (1 + x)^2 - (x^2 - 1)^2/4$ and $\mathbf{K}(m)$ for the complete elliptic integral of the first kind, and $E^{\pm\pm}(x)$ is given by (7) with the substitution $\epsilon_\mathbf{k} \to x$.

Appendix C. The cyclotron mass

On the basis of the full tight-binding band structure $E_\mathbf{k}^{\pm\pm}$ given in (7) it is possible to derive general expressions for the cyclotron mass (26). The key observation is that the area of a closed orbit at the Fermi level $A(E_F)$ may be written as $A(E_F) \propto \sum_\mathbf{k}' \Delta_\mathbf{k}$, where the prime means summation over all $\mathbf{k}$s inside the orbit, and $\Delta_\mathbf{k} = (2\pi)^2/(N_c A_\bigcirc)$ is the area per k-point in the first BZ. The cyclotron mass may then be written as $m_c \propto \partial_{E_F} \sum_i \xi_i \int_{\mathcal{E}_i}^{E_F} dE \sum_\mathbf{k} \delta(E - E_\mathbf{k}^{\mu\nu})\Theta(\epsilon^\pm - \epsilon_\mathbf{k})$, where $\epsilon_\mathbf{k}$ is the SLG dispersion, $\xi_i = \pm$, and $\epsilon^\pm = [E_F^2 + V^2/4 \pm \sqrt{E_F^2(V^2 + t_\perp^2) - t_\perp^2 V^2/4}]^{\frac{1}{2}}$. The integration limits $\mathcal{E}_i$, the sign $\xi_i = \pm$, and the choice between the two possibilities $\epsilon^\pm$ depend on the particular band and on the position of the Fermi level. Skipping the details of the derivation, what is worth noting is that, due to the sum of delta functions in the previous expression for m_c, the result has a mathematical structure similar to those of the derived expressions for the DOS of BLG (see appendix B). The cyclotron effective mass of the biased BLG for the relevant parameter range $V \lesssim t_\perp \ll t$ and $|E_F| \lesssim t$ is then given by

$$m_c(E_F) = \frac{\hbar^2}{A_\bigcirc t^2} \frac{2}{\pi} \begin{cases} -\psi^{--}(E_F)\mathcal{F}^-(E_F), & \\ \quad \Delta_g/2 < |E_F| < V/2 \\ \psi^{-+}(E_F)\mathcal{F}^+(E_F), & \\ \quad \Delta_g/2 < |E_F| \lesssim t \\ \psi^{+-}(E_F)\mathcal{F}^-(E_F), & \\ \quad \sqrt{t_\perp^2 + V^2/4} < |E_F| \lesssim t, \end{cases}$$
$$(C.1)$$

with $\mathcal{F}^l(E_F)$ as in (B.4).

References

[1] McCann E, Abergel D S L and Fal'ko V I 2007 *Solid State Commun.* **143** 110
[2] McCann E, Abergel D S L and Fal'ko V I 2007 *Eur. Phys. J. Spec. Top.* **148** 91–103
[3] Abergel D S L and Fal'ko V I 2007 *Phys. Rev.* B **75** 155430
[4] Guinea F, Castro Neto A and Peres N 2007 *Solid State Commun.* **143** 116–22
[5] Castro Neto A H, Guinea F, Peres N M R, Novoselov K S and Geim A K 2009 *Rev. Mod. Phys.* **81** 109
[6] Novoselov K S, McCann E, Morozov S V, Fal'ko V I, Katsnelson M I, Zeitler U, Jiang D, Schedin F and Geim A K 2006 *Nat. Phys.* **2** 177–80
[7] McCann E and Fal'ko V I 2006 *Phys. Rev. Lett.* **96** 086805
[8] Ohta T, Bostwick A, Seyller T, Horn K and Rotenberg E 2006 *Science* **313** 951

[9] Oostinga J B, Heersche H B, Liu X, Morpurgo A F and Vandersypen L M K 2008 *Nat. Mater.* **7** 151–7
[10] Castro E V, Novoselov K S, Morozov S V, Peres N M R, Lopes dos Santos J M B, Nilsson J, Guinea F, Geim A K and Castro Neto A H 2007 *Phys. Rev. Lett.* **99** 216802
[11] Guinea F, Castro Neto A H and Peres N M R 2006 *Phys. Rev. B* **73** 245426
[12] McCann E 2006 *Phys. Rev. B* **74** 161403(R)
[13] Min H, Sahu B, Banerjee S K and MacDonald A H 2007 *Phys. Rev. B* **75** 155115
[14] Aoki M and Amawashi H 2007 *Solid State Commun.* **142** 123–7
[15] Guinea F 2007 *Phys. Rev. B* **75** 235433
[16] Mak K F, Lui C H, Shan J and Heinz T F 2009 *Phys. Rev. Lett.* **102** 256405
[17] Zhang Y, Tang T T, Girit C, Hao Z, Martin M C, Zettl A, Crommie M F, Shen Y R and Wang F 2009 *Nature* **459** 820–3
[18] Nilsson J, Castro Neto A H, Guinea F and Peres N M R 2006 *Phys. Rev. Lett.* **97** 266801
[19] Morozov S V, Novoselov K S, Katsnelson M I, Schedin F, Elias D, Jaszczak J A and Geim A K 2008 *Phys. Rev. Lett.* **100** 016602
[20] Koshino M and Ando T 2006 *Phys. Rev. B* **73** 245403
[21] Katsnelson M I 2006 *Eur. Phys. J.* B **51** 157–60
[22] Katsnelson M I 2006 *Eur. Phys. J.* B **52** 151–3
[23] Cserti J 2007 *Phys. Rev. B* **75** 033405
[24] Cserti J, Csordás A and Dávid G 2007 *Phys. Rev. Lett.* **99** 066802
[25] Snyman I and Beenakker C W J 2007 *Phys. Rev. B* **75** 045322
[26] Katsnelson M and Novoselov K 2007 *Solid State Commun.* **143** 3–13
[27] Nilsson J, Castro Neto A H, Guinea F and Peres N M R 2007 *Phys. Rev. B* **76** 165416
[28] Pereira J M Jr, Vasilopoulos P and Peeters F M 2007 *Nano Lett.* **7** 946–9
[29] Nilsson J and Castro Neto A H 2007 *Phys. Rev. Lett.* **98** 126801
[30] Castro E V, Peres N M R and Lopes dos Santos J M B 2007 *Phys. Status Solidi* b **244** 2311
[31] Nilsson J, Castro Neto A H, Guinea F and Peres N M R 2008 *Phys. Rev. B* **78** 045405
[32] Lopes dos Santos J M B, Peres N M R and Castro Neto A H 2007 *Phys. Rev. Lett.* **99** 256802
[33] Hass J, Varchon F, Millán-Otoya J E, Sprinkle M, Sharma N, de Heer W A, Berger C, First P N, Magaud L and Conrad E H 2008 *Phys. Rev. Lett.* **100** 125504
[34] Stauber T, Peres N M R, Guinea F and Castro Neto A H 2007 *Phys. Rev. B* **75** 115425
[35] Castro E V, Peres N M R, Stauber T and Silva N A P 2008 *Phys. Rev. Lett.* **100** 186803
[36] Pereira J M Jr, Peeters F M and Vasilopoulos P 2007 *Phys. Rev. B* **76** 115419
[37] Semenov Y G, Zavada J M and Kim K W 2008 *Phys. Rev. B* **77** 235415
[38] Raza H and Kan E C 2009 *J. Phys.: Condens. Matter* **21** 102202
[39] Novoselov K, Geim A, Morozov S, Jiang D, Katsnelson M, Grigorieva I, Dubonos S and Firsov A 2005 *Nature* **438** 197
[40] Toy W W, Dresselhaus M S and Dresselhaus G 1977 *Phys. Rev. B* **15** 4077–90
[41] Malard L M, Nilsson J, Elias D C, Brant J C, Plentz F, Alves E S, Castro Neto A H and Pimenta M A 2007 *Phys. Rev. B* **76** 201401(R)
[42] Misu A, Mendez E E and Dresselhaus M S 1979 *J. Phys. Soc. Japan* **47** 199–207
[43] Charlier J C, Gonze X and Michenaud J P 1991 *Phys. Rev. B* **43** 4579–89
[44] McClure J W 1957 *Phys. Rev.* **108** 612–8
[45] Slonczewski J C and Weiss P R 1958 *Phys. Rev.* **109** 272–9
[46] Peres N M R, Guinea F and Castro Neto A H 2006 *Phys. Rev. B* **73** 125411

[47] Partoens B and Peeters F M 2006 *Phys. Rev.* B **74** 075404
[48] Kuzmenko A B, Crassee I, van der Marel D, Blake P and Novoselov K S 2009 *Phys. Rev. B* **80** 165406
[49] Zhang L M, Li Z Q, Basov D N, Fogler M M, Hao Z and Martin M C 2008 *Phys. Rev. B* **78** 235408
[50] Li Z Q, Henriksen E A, Jiang Z, Hao Z, Martin M C, Kim P, Stormer H L and Basov D N 2009 *Phys. Rev. Lett.* **102** 037403
[51] Reich S, Maultzsch J, Thomsen C and Ordejón P 2002 *Phys. Rev. B* **66** 035412
[52] Nilsson J, Castro Neto A H, Peres N M R and Guinea F 2006 *Phys. Rev. B* **73** 214418
[53] Mañes J L, Guinea F and Vozmediano M A H 2007 *Phys. Rev.* B **75** 155424
[54] Zhou S Y, Siegel D A, Fedorov A V and Lanzara A 2008 *Phys. Rev. Lett.* **101** 086402
[55] Zhang Y, Tan Y W, Stormer H L and Kim P 2005 *Nature* **438** 201–4
[56] Schedin F, Geim A K, Morozov S V, Hill E W, Blake P, Katsnelson M I and Novoselov K S 2007 *Nat. Mater.* **6** 652–5
[57] Moser J, Verdaguer A, Jimenez D, Barreiro A and Bachtold A 2008 *Appl. Phys. Lett.* **92** 123507
[58] Ribeiro R M, Peres N M R, Coutinho J and Briddon P R 2008 *Phys. Rev. B* **78** 075442
[59] Boukhvalov D W and Katsnelson M I 2008 *Phys. Rev.* B **78** 085413
[60] de Heer W A, Berger C, Wu X, First P N, Conrad E H, Li X, Li T, Sprinkle M, Hass J, Sadowski M L, Potemski M and Martinez G 2007 *Solid State Commun.* **143** 92–100
[61] Varchon F, Feng R, Hass J, Li X, Nguyen B N, Naud C, Mallet P, Veuillen J Y, Berger C, Conrad E H and Magaud L 2007 *Phys. Rev. Lett.* **99** 126805
[62] Mattausch A and Pankratov O 2007 *Phys. Rev. Lett.* **99** 076802
[63] Kim S, Ihm J, Choi H J and Son Y W 2008 *Phys. Rev. Lett.* **100** 176802
[64] Varchon F, Mallet P, Veuillen J Y and Magaud L 2008 *Phys. Rev. B* **77** 235412
[65] Mallet P, Varchon F, Naud C, Magaud L, Berger C and Veuillen J Y 2007 *Phys. Rev. B* **76** 041403
[66] Rutter G M, Guisinger N P, Crain J N, Jarvis E A A, Stiles M D, Li T, First P N and Stroscio J A 2007 *Phys. Rev. B* **76** 235416
[67] Brar V W, Zhang Y, Yayon Y, Bostwick A, Ohta T, McChesney J L, Horn K, Rotenberg E and Crommie M F 2007 *Appl. Phys. Lett.* **91** 122102
[68] Jang C, Adam S, Chen J H, Williams E D, Das Sarma S and Fuhrer M S 2008 *Phys. Rev. Lett.* **101** 146805
[69] Kusminskiy S V, Nilsson J, Campbell D K and Castro Neto A H 2008 *Phys. Rev. Lett.* **100** 106805
[70] Tersoff J and Hamann D R 1985 *Phys. Rev. B* **31** 805–13
[71] Haydock R 1980 The recursive solution of the Schrödinger equation *Solid State Physics* vol 35 ed H Ehrenreich, F Seitz and D Turnbull (New York: Academic) p 215
[72] Wang Z F, Li Q, Su H, Wang X, Shi Q W, Chen J, Yang J and Hou J G 2007 *Phys. Rev. B* **75** 085424
[73] Bena C 2008 *Phys. Rev. Lett.* **100** 076601
[74] Lin Y M and Avouris P 2008 *Nano Lett.* **8** 2119
[75] Lifshitz I M and Kaganov M I 1980 Geometric concepts in the electron theory of metals *Electrons at the Fermi Surface* ed M Springford (Cambridge: Cambridge University Press) chapter 1, pp 3–45
[76] Landau L D and Lifshitz I M 1980 *Statistical Physics Part 2* vol 9 (Oxford: Pergamon)
[77] Ziman J M 1972 *Principles of the Theory of Solids* 2nd edn (Cambridge: Cambridge University Press)
[78] Misumi T and Shizuya K 2008 *Phys. Rev. B* **77** 195423
[79] Nakamura M, Hirasawa L and Imura K I 2008 *Phys. Rev. B* **78** 033403
[80] Henriksen E A, Jiang Z, Tung L C, Schwartz M E, Takita M, Wang Y J, Kim P and Stormer H L 2008 *Phys. Rev. Lett.* **100** 087403
[81] Kusminskiy S V, Campbell D K and Castro Neto A H 2009 *Europhys. Lett.* **85** 58005